JACS
JOURNAL OF THE AMERICAN CHEMICAL SOCIETY
pubs.acs.org/JACS
Article

In Situ Surface Structures of PdAg Catalyst and Their Influence on Acetylene Semihydrogenation Revealed by Machine Learning and Experiment

Xiao-Tian Li,[†] Lin Chen,[†] Cheng Shang, and Zhi-Pan Liu*

Cite This: *J. Am. Chem. Soc.* 2021, 143, 6281−6292
Read Online
ACCESS | Metrics & More | Article Recommendations | Supporting Information

ABSTRACT: PdAg alloy is an industrial catalyst for acetylene-selective hydrogenation in excess ethene. While significant efforts have been devoted to increase the selectivity, there has been little progress in the catalyst performance at low temperatures. Here by combining a machine-learning atomic simulation and catalysis experiment, we clarify the surface status of PdAg alloy catalyst under the reaction conditions and screen out a rutile-TiO_2 supported Pd_1Ag_3 catalyst with high performance: i.e., 85% selectivity at >96% acetylene conversion over a 100 h period in an experiment. The machine-learning global potential energy surface exploration determines the Pd-Ag-H bulk and surface phase diagrams under the reaction conditions, which reveals two key bulk compositions, Pd_1Ag_1 ($R\bar{3}m$) and Pd_1Ag_3 ($Pm\bar{3}m$), and quantifies the surface structures with varied Pd:Ag ratios under the reaction conditions. We show that the catalyst activity is controlled by the PdAg patterns on the (111) surface that are variable under reaction conditions, but the selectivity is largely determined by the amount of Pd exposure on the (100) surface. These insights provide the fundamental basis for the rational design of a better catalyst via three measures: (i) controlling the Pd:Ag ratio at 1:3, (ii) reducing the nanoparticle size to limit PdAg local patterns, (iii) searching for active supports to terminate the (100) facets.

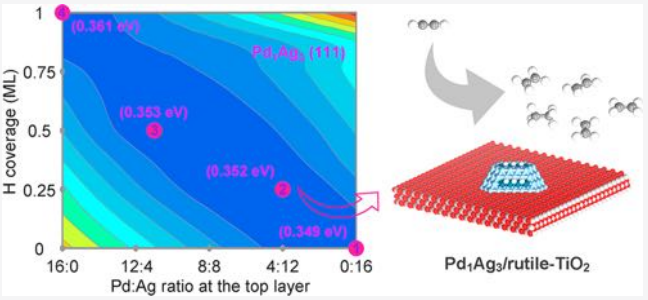

1. INTRODUCTION

PdAg alloy is known to be the best low-temperature catalyst for the selective hydrogenation of acetylene (HCCH) in excess ethene, an important heterogeneous catalytic process in the petroleum industry.[1−9] To date, the typical selectivity is ∼55% at >90% acetylene conversion under industrial conditions (<100 °C),[10−16] which is already much better than those for the pure Pd catalyst that has essentially no selectivity due to the strong preference of converting ethene to ethane, the fully hydrogenated product. While there is consensus that Pd is the active component in the alloy, many uncertainties persist regarding the role of Ag. A common view has been that Ag prevents the formation of the active PdH_x phases under the reaction conditions, which are responsible for the ethene hydrogenation.[2,17−20] It was also argued that the alloying may dilute the Pd ensemble and thus affect the hydrogenation kinetics by altering the adsorption strength of acetylene and ethene.[6−8] Nevertheless, since the presence of Ag is critical to the selectivity, significant efforts have been focused on the synthesis of other Pd alloys (e.g., Pd-Ga,[21−23] Pd-In,[24,25] and Pd-Zn[26,27]); however, limited progress has been achieved in the low-temperature conversion.

Although PdAg alloy has long been known to form a face-centered-cubic (fcc) solid solution at all compositions when it is annealed below ∼900 °C,[28] it is elusive whether there is Pd-Ag short-range ordering due to the similar atomic scattering factors of Pd and Ag.[28,29] Therefore, for the PdAg catalysts in acetylene hydrogenation, which are generally treated below 600 °C, there is much uncertainty on the local PdAg pattern. Surface science studies by scanning tunneling microscopy (STM)[30] demonstrated that the surface segregation of Ag[31,32] is possible: Ag can be enriched on both (111) and (100) for a Pd_2Ag_1 alloy annealed at high temperature (497−547 °C) under vacuum. Similarly, a recent work combining STM, spectroscopy, and machine-learning molecular dynamics[33] showed the reconstruction of Pd islands deposited on Ag(111), where Ag atoms gradually migrate out of the surface and climb on the Pd islands at only 177 °C. To date, no *in situ* data, however, are available for the PdAg catalysts during acetylene hydrogenation, where the reaction generally occurs below 100 °C in the feed gas of H_2. Adsorbates such as H could be the additional variant to alter the surface segregation behavior.[34]

Received: March 5, 2021
Published: April 20, 2021

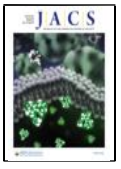

https://doi.org/10.1021/jacs.1c02471
J. Am. Chem. Soc. 2021, 143, 6281−6292

Density functional theory (DFT) calculations have provided some insights into the interaction of the reactants with PdAg surfaces,[1,35−40] on the basis of the idealized crystal surface models truncated from the alloy bulk. The conclusions are mostly consistent with the knowledge from experiments: for example, (i) ethene, with a double bond, adsorbs much more weakly in comparison to acetylene, which has a triple bond, (ii) the C-containing species prefer to bond with Pd, instead of Ag, and thus the adsorption strength decreases with an increase in surface Ag content, and (iii) while the d-band states of Pd and Ag are very different, the Pd d-band has only a slight shift after Ag alloying, implying a minor influence on the Pd electronic structure. For the catalytic reactions, by calculating the hydrogenation process on PdAg(111) and Pd(111), Studt et al.[1] found that the presence of Ag primarily alters the adsorption energy rather than the activation energy, and thus they concluded that the weaker adsorption strength of ethene on PdAg helps to suppress the deep hydrogenation. As the previous theoretical models are simplified, many key questions in the field remain open such as the following, to name a few. Is the formation of PdH_x phases inhibited by Ag? Does the surface Pd:Ag ratio vary during the hydrogenation reaction? How do the activity and selectivity depend on the position of Ag?

Our recent work has investigated the acetylene hydrogenation on pure Pd catalyst by combining a machine-learning atomic simulation and experiment.[20] We found that it is the more open Pd(100) surface that provides the lowest energy channel for ethene hydrogenation. The formation of PdH_x is not the major cause of the low selectivity of Pd, although PdH_x(100) is indeed even more nonselective than Pd(100). For pure Pd catalyst, the large nanoparticles dominated by the (111) surface do improve significantly the selectivity.

Here we focus on the acetylene hydrogenation on PdAg alloy, aiming to clarify the PdAg surface structures under the catalytic conditions and design a better catalyst for acetylene hydrogenation. The first four-element Pd-Ag-C-H global neural network (G-NN) potential has been constructed that allows for fast exploration of the vast global structure and reaction space in acetylene hydrogenation. Two key thermodynamically stable bulks, Pd_1Ag_1 ($R\bar{3}m$) and Pd_1Ag_3 ($Pm\bar{3}m$) are thus identified, from which the likely surface structure patterns are determined on (111) and (100) surfaces. On the basis of catalysis experiments and microkinetic simulation, we demonstrate that the Pd_1Ag_3 catalyst achieves the best performance, since its (100) surface could be entirely blocked by Ag. The (111) surface of Pd_1Ag_3 evolves slowly under the reaction conditions by accumulating Pd onto the surface layer, which leads to a decrease in conversion while the selectivity is maintained. With these fundamental insights, we screened out a rutile-TiO_2 supported Pd_1Ag_3 catalyst, which achieves 85% selectivity at >96% acetylene conversion over a long catalyst test.

2. METHODS

2.1. SSW-NN Simulation. The stochastic surface walking based on the global neural network potential (SSW-NN) method, as implemented in large-scale atomic simulation with neural network potential (LASP) code,[41] was utilized for fast global potential energy surface (PES) exploration to resolve the bulk and surface structures during the reactions.[20,42−47] The Pd-Ag-C-H quaternary element G-NN potential was developed by self-learning the DFT global PES data set, which was generated from the SSW global PES exploration[48−50] for systems with different Pd-Ag-C-H compositions/structures. The self-learning was performed iteratively until the G-NN potential was robust enough to describe the global PES quantitatively. The procedure is briefly introduced below, and more details can be found in Section 1 in the Supporting Information.

The global PES data set was generated iteratively by the SSW simulations on all types of structures (including cluster, layer, and bulk) with a series of different Pd-Ag-C-H compositions and varied supercells up to 121 atoms/cell (see Table S1 in the Supporting Information). The first-round data set came from a DFT-based SSW simulation, while the others were from an NN-based SSW simulation in the self-learning. More than 10^7 structures were generated in total, and 55213 of them were selected and calculated by DFT calculations as the final global data set for G-NN potential training.

The G-NN potential was established using the artificial neural network technique based on the global data set, as described previously.[51−54] To pursue a high accuracy for the PES, a large set of power-type structure descriptors (PTSD) were adopted for each element, including 151 two-body descriptors, 230 three-body descriptors, and 12 four-body descriptors. In addition, a large neural network involving two hidden layers (393−60−60−1), 82083 network parameters in total, was utilized, where the hyperbolic tangent was utilized as the activation function for the hidden layers while the linear function was utilized for the output layer. The energy, force, and stress were matched to DFT calculations with the root-mean-square errors (RMSE) being 3.25 meV, 0.055 eV/Å, and 0.434 GPa, respectively. A systematic benchmark was performed against the DFT results, showing good accuracy of the G-NN potential. For example, we have computed the energy difference between G-NN and DFT calculations for 1602 Pd-Ag-H surface structures, which shows a low RMSE of 4.9 meV/atom as seen in Figure S1 in the Supporting Information. A detailed comparison between G-NN and DFT calculations for the hydrogenation reaction is also compiled in Table S2 in the Supporting Information.

2.2. Surface Models and Transition State Search. To model the surfaces, we generally adopted four-layer slabs, a $(4 \times 2\sqrt{3})$ supercell for modeling (111) and a (4×4) supercell for modeling (100). In the calculations of surface compositions, the bottom three layers were constructed from the bulk-truncated structure, while the top layer was allowed to vary in Pd:Ag ratio and H coverage. The results were utilized to plot the Pd-Ag-H contour maps on the basis of the computed surface formation free energy (see below). In the simulation of chemical reactions, the bottom two layers were kept fixed while the top two layers were allowed to fully relax.

The double-ended surface walking (DESW) method[55,56] was utilized to locate the transition states (TS) for the hydrogenation reactions. This was achieved by driving two images from the initial state (IS) and final state (FS) toward each other via the consecutive addition of bias Gaussian potential. After the path was connected, the constrained Broyden dimer (CBD) method[57,58] starting from the maximum energy point along the path was then utilized to locate the TSs, which were further confirmed by vibrational frequency calculations and an extrapolation optimization to the correct IS and FS. To address the activity and selectivity in comparison with experiment, we have further converged all the pathways by DFT, and all the data reported in this work without explicit mention are from DFT calculations.

2.3. DFT Calculations. The DFT calculations were performed using the periodic plane-wave method with the projected augmented wave (PAW)[59] scheme, as implemented in the Vienna ab initio simulation package (VASP).[60] The Perdew−Burke−Ernzerhof (PBE) functional at the generalized gradient approximation (GGA)[61] was employed for all of the calculations with a plane-wave basis set at a 450 eV cutoff. The Monkhorst−Pack *k*-mesh was 30 times the reciprocal lattice vectors ($1/30$ Å^{-1}), and the convergence criterion for the atomic force was set to be 0.01 eV/Å. Density functional perturbation theory was utilized for the calculation of phonon spectra to determine the zero-point energy (ZPE).

To obtain the free energy profile, we have calculated the Gibbs free energy for all of the states on the basis of the ZPE-corrected DFT total energy, which was set as the enthalpy at 0 K. The free energy of the gas-phase molecules was computed from thermodynamics by utilizing the standard thermodynamics data at the standard state[62] (e.g., the standard state G(25 °C, 1 bar) values for acetylene, ethene, ethane, and

https://doi.org/10.1021/jacs.1c02471
J. Am. Chem. Soc. 2021, 143, 6281−6292

hydrogen are −0.52, −0.57, −0.60, and −0.32 eV, respectively). The adsorption barrier of the molecule was estimated by the entropy difference before and after adsorption. For the adsorbate on the surface, the free energy was approximated as the enthalpy at 0 K, since the thermal effect of enthalpy and the entropy dependence on temperature are small.[63]

2.4. Experimental Methods. *2.4.1. Synthesis of PdAg Catalysts.* The PdAg catalysts were synthesized by a coimpregnation method and loaded on MgAl hydrotalcite (HT). The HT was first calcined in air at 400 °C for 6 h to improve its hydrophilicity and then was dispersed in 2 mL of water in a bottle. After sonication for 10 min and stirring for 30 min, the precursor $(Pd(NO_3)_2{\cdot}2H_2O$ and $AgNO_3$ solution) was added quickly to the mixture, with continuous stirring for 6 h. Thereafter, the sample was dried in air at 90 °C for 12 h and calcined in air at 450 °C for 4 h. Finally, after reduction in 5% H_2/Ar at 400 °C for 5 h, the PdAg/HT catalysts were prepared. The other catalysts, including Pd/HT and various PdAg nanoparticles on different supports (α-Al_2O_3, γ-Al_2O_3, SiO_2, Y_2O_3, $CaCO_3$, rutile-TiO_2 (r-TiO_2), anatase-TiO_2 (a-TiO_2), the commercial TiO_2 mixed phase (P25), and the mesoporous titanosilicates Ti-MWW, were prepared similarly (see also the Supporting Information for more information).

2.4.2. Hydrogenation Reaction Experiment. The hydrogenation reactions were performed in a continuous flow fixed-bed microreactor. For uniformity, all of the samples contained 0.25 mg of Pd, mixed with 20 g of green silicon carbide. The gas consisted of 0.5% C_2H_2, 50.0% C_2H_4, 5.0% H_2, 4.0% He, and 40.5% N_2, fed at a flow rate of 40 mL/min. Prior to the reaction, the catalysts were pretreated in 5% H_2/Ar at 150 °C for 3 h and then cooled to the reaction temperature. The products were analyzed by an online gas chromatograph (GC, Agilent 7890B) that was equipped with two thermal conductivity detectors (TCD) and a flame ionization detector (FID). The activity and selectivity of the catalysts were evaluated from the steady data (after 1 h in stream) by

$$C_{\text{acetylene}} = \frac{C_2H_{2(\text{in})} - C_2H_{2(\text{out})}}{C_2H_{2(\text{in})}} \times 100\% \quad (1)$$

$$S_{\text{ethene}} = \left(1 - \frac{C_2H_{6(\text{out})} - C_2H_{6(\text{in})}}{C_2H_{2(\text{in})} - C_2H_{2(\text{out})}}\right) \times 100\% \quad (2)$$

3. RESULTS

3.1. PdAg Bulk. A good knowledge of the *in situ* structure is the first step to understand the catalytic kinetics of PdAg catalysts. We start our investigations from the bulk phase of PdAg by using the SSW-NN method to explore the global PES of Pd-Ag-H with different compositions. We first rule out the $PdAgH_x$ hydride bulk phases (e.g., $Pd_1Ag_1H_{0.5}$), the dissolution of H in PdAg bulk,[20] since they are less stable in comparison to the corresponding PdAg and the gas-phase H_2 (the typical reaction conditions of 25 °C and $p(H_2) = 0.05$ atm were utilized to compute the free energy of H_2).

We now focus on the Pd-Ag phase diagram determined from SSW-NN, as summarized in the thermodynamics convex hull plot in Figure 1a. We find that the alloying of Pd and Ag is exothermic at all compositions with respect to the Pd and Ag metal, and the alloys generally prefer the fcc lattice, the same as the Pd and Ag metals. It should be noted that the formation energies of PdAg alloys are generally small (only up to −0.06 eV/atom at Pd/Ag = 1/1), implying a weak interaction between Pd and Ag. This fact explains the experimental observation of the PdAg solid solution with random ordering at high temperatures.[28]

Five convex configurations can be resolved from Figure 1a, which are Pd_1Ag_1 ($R\bar{3}m$, −0.060 eV/atom), Pd_5Ag_{11} ($C2/m$, −0.060 eV/atom), Pd_1Ag_3 ($Pm\bar{3}m$, −0.055 eV/atom), Pd_3Ag_{13} ($I4/mmm$, −0.045 eV/atom), and Pd_1Ag_7 ($P4/mmm$, −0.032 eV/atom), as indicated by open circles in the figure. Among them, the atomic structures of Pd_1Ag_1 and Pd_1Ag_3 are representative, since the other alloy structures can be considered as a mix of these two structures and pure Ag. For Pd_1Ag_1, the crystal has alternating Pd and Ag layers along the close-packed [111] direction, while for Pd_1Ag_3, Pd atoms are uniformly distributed with Ag atoms. Importantly, we note that it is not possible to infinitely separate Pd atoms in an Ag matrix: the largest separation is achieved in Pd_1Ag_3, where Pd atoms can only be located as the second nearest neighbors to each Pd atom.

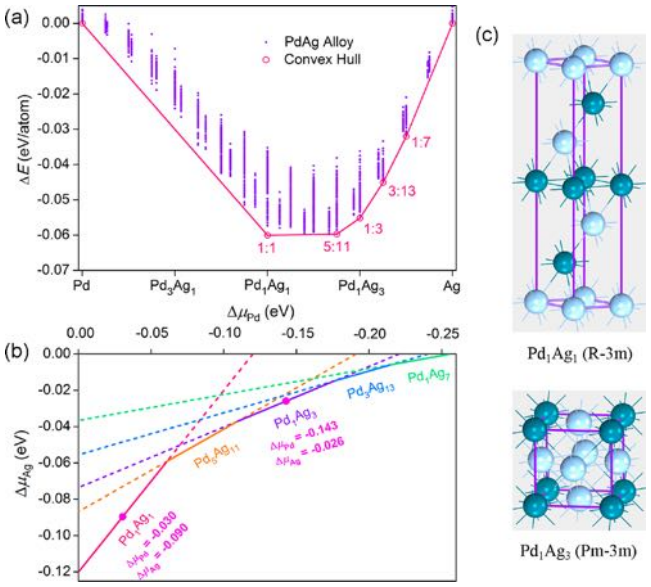

Figure 1. (a) Convex hull diagram of PdAg alloy bulk with respect to pure Pd and Ag metal. The open circles denote the convex configurations. (b) Excess of chemical potentials of Pd and Ag in forming PdAg alloy, with respect to the Pd and Ag metals. Each convex Pd-Ag composition corresponds to a linear line in the figure, where the excesses of chemical potentials $\Delta\mu_{Pd}$ and $\Delta\mu_{Ag}$ for two key compositions, Pd_1Ag_1 and Pd_1Ag_3, are identified. (c) Atomic crystal structures of two key convex configurations: Pd_1Ag_1 ($R\bar{3}m$, a = 2.85 Å, c = 14.00 Å) and Pd_1Ag_3 ($Pm\bar{3}m$, a = 4.09 Å). Color code: Pd, indigo balls; Ag, light blue balls.

In order to identify the chemical potentials of Pd and Ag in forming PdAg alloys, we transform Figure 1a into Figure 1b by considering eq 3

$$\Delta E_{\text{bulk}} = \Delta\mu_{\text{Pd}} N_{\text{Pd}} + \Delta\mu_{\text{Ag}} N_{\text{Ag}} \quad (3)$$

where ΔE_{bulk} for a composition can be read from Figure 1a (e.g., $\Delta E_{\text{bulk}}(Pd_1Ag_1) = -0.06$ eV/atom); $\Delta\mu_{Pd}$ and $\Delta\mu_{Ag}$ are the excesses of chemical potentials of Pd and Ag with respect to the Pd and Ag metals, respectively, and are utilized as the variables in the axes of Figure 1b. Each composition will therefore correspond to a linear line in the figure, and consistently, the five thermodynamically stable compositions, Pd_1Ag_1, Pd_5Ag_{11}, Pd_1Ag_3, Pd_3Ag_{13}, and Pd_1Ag_7, are identified as five segments with the lowest ΔE_{bulk} values. We can obtain the average $\Delta\mu_{Pd}$ and $\Delta\mu_{Ag}$ values for each composition from the figure. For example, by using the midpoints of the segments, we obtain $\Delta\mu_{Pd} = -0.030$ eV and $\Delta\mu_{Ag} = -0.090$ eV for Pd_1Ag_1 ($R\bar{3}m$) and $\Delta\mu_{Pd} = -0.143$ eV and $\Delta\mu_{Ag} = -0.026$ eV for Pd_1Ag_3 ($Pm\bar{3}m$). These values pin the chemical potentials of Pd and Ag in the PdAg alloy bulk and thus can be utilized to determine the free energy of the surface structures.

https://doi.org/10.1021/jacs.1c02471
J. Am. Chem. Soc. 2021, 143, 6281−6292

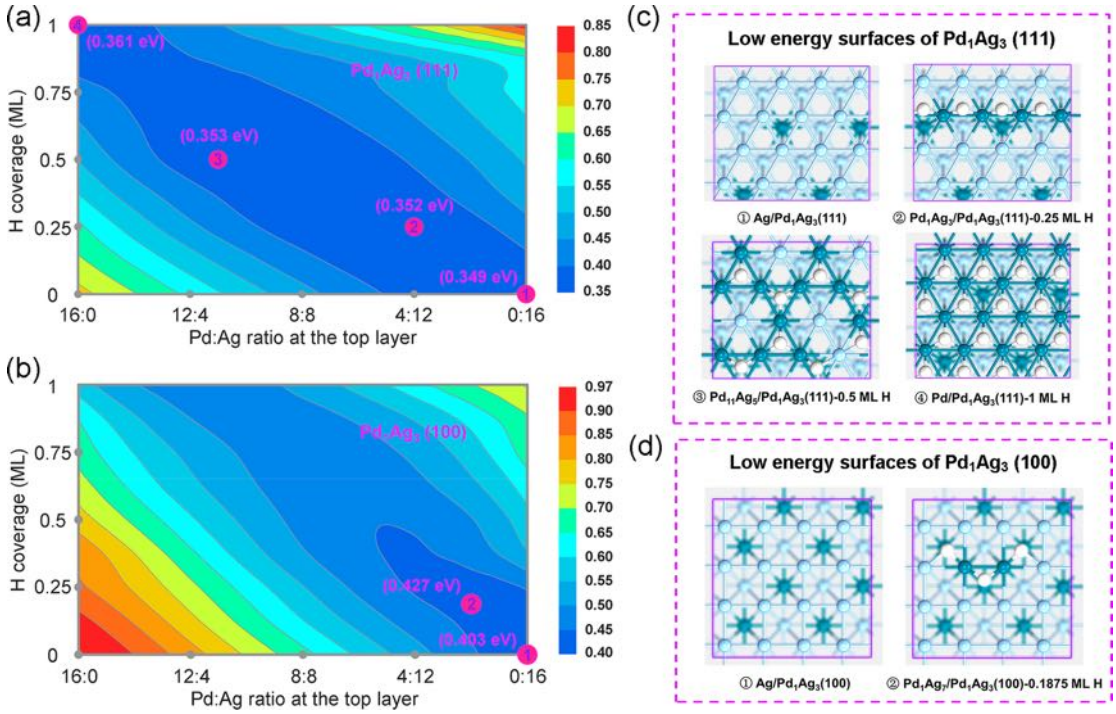

Figure 2. (a, b) Pd-Ag-H surface contour maps for the formation free energies of Pd-Ag-H/Pd_1Ag_3(111) and Pd-Ag-H/Pd_1Ag_3(100), at 25 °C and $p(H_2)$ = 0.05 atm. The formation free energy here is averaged to each metal atom at the top layer. (c, d) Stable surface configurations of Pd_1Ag_3(111) and Pd_1Ag_3(100) under the typical reaction conditions, as determined from the Pd-Ag-H surface contour maps.

3.2. PdAg Surface. We now explore the surface structures of Pd_1Ag_1 and Pd_1Ag_3 based on their PdAg bulk crystals. By setting the typical reaction conditions (i.e. 25 °C and $p(H_2)$ = 0.05 atm) that define the chemical potential of H, we can determine the thermodynamics at different surface compositions during the reaction. The SSW-NN global optimization was utilized to search for the possible structures of (111) and (100) surfaces of Pd_1Ag_1 and Pd_1Ag_3 (the calculation details can be found in Methods).

The stability of the surface is measured by the free energy excess ΔG_{sur}, with respect to the Pd and Ag components in the bulk, as shown in Figure 2. ΔG_{sur} is defined by eq 4

$$\Delta G_{sur} = (E_{sur} + ZPE_H N_H) - (G_{Pd} + \Delta\mu_{Pd})N_{Pd} - (G_{Ag} + \Delta\mu_{Ag})N_{Ag} - \mu_H N_H \quad (4)$$

where μ_H is set as half of H_2 at 25 °C and 0.05 atm, G_{Pd} and G_{Ag} are the total energies of Pd and Ag metal, respectively, $\Delta\mu_{Pd}$ and $\Delta\mu_{Ag}$ for each alloy composition can be found from Figure 1b, E_{sur} is the total energy of the slab, ZPE_H is the zero-point energy for the adsorbed H, and N_{Pd}, N_{Ag}, and N_H are the numbers of Pd, Ag, and H atoms in the slab.

Figure 2a,b shows the Pd-Ag-H contour maps for Pd-Ag-H/Pd_1Ag_3(111) and Pd-Ag-H/Pd_1Ag_3(100) at different surface Pd/Ag ratios and H coverages. In general, for both (111) and (100) without H, we find that the Ag-exposed surfaces have the highest stability, which appear at the bottom right corners in the contour maps. This indicates the preference of Ag segregation on the surfaces of Pd_1Ag_3 due to the lower surface energy of the Ag element. Under the reaction conditions where H atoms are populated, however, the Ag surface segregation is largely inhibited, since a number of possible Pd-exposed surface structures are energetically nearly degenerate with the Ag-covered surface. In particular, on the (111) surface, these low-energy structures form a long valley at different Pd/Ag compositions (Figure 2a), from zero H coverage to a full monolayer (ML) coverage, with the formation free energy only differing by 0.012 eV, as also shown in Figure 2c. Interestingly, the valley on (100) is much smaller and, correspondingly, the H coverage is only up to 0.25 ML.

Now we can have a close look at the low-energy surface structures. Figure 2c shows four selected surface configurations of Pd_1Ag_3(111). The most stable configuration (0.349 eV) has a full Ag exposure, denoted as Ag/Pd_1Ag_3(111), where the symbol / separates the composition at the first and the bottom layers; Pd_1Ag_3/Pd_1Ag_3(111)-0.25 ML H is a representative structure with the surface Pd atoms arranged in a line (Pd line ensemble), where the H atoms adsorb at the bridge of two Pd atoms. Its formation free energy is slightly higher than that of Ag/Pd_1Ag_3(111) by 0.003 eV; with more Pd atoms accumulating to the top layer, e.g. $Pd_{11}Ag_5$/Pd_1Ag_3(111)-0.5 ML H, the local Pd_3 ensemble forms and the H atoms adsorb at the 3-fold Pd hollow sites. The structure is 0.004 eV less stable in comparison to the Ag-covered surface (Ag/Pd_1Ag_3(111)); finally, the Pd/Pd_1Ag_3(111)-1 ML H configuration has a full layer exposure of Pd with a full layer of adsorbed H (Pd layer ensemble). Its formation free energy is 0.012 eV higher than that of the Ag-covered surface. From these stable surface structures, one can conclude that H prefers to bond to Pd atoms with at least two coordinations, which induces the appearance of Pd atoms onto the surface.

The situation on (100) is quite similar to that of (111), except that (100) has a much higher cost for Pd exposure. This is apparently due to the lower coordinations of (100) that favors more the low-surface-energy Ag metal. Figure 2d shows two typical low-surface-energy configurations, the Ag-covered configuration and that with Pd/Ag = 1/7 at the top layer. The latter, Pd_1Ag_7/Pd_1Ag_3(100)-0.1875 ML H, having a surface Pd_2

https://doi.org/10.1021/jacs.1c02471
J. Am. Chem. Soc. 2021, 143, 6281−6292

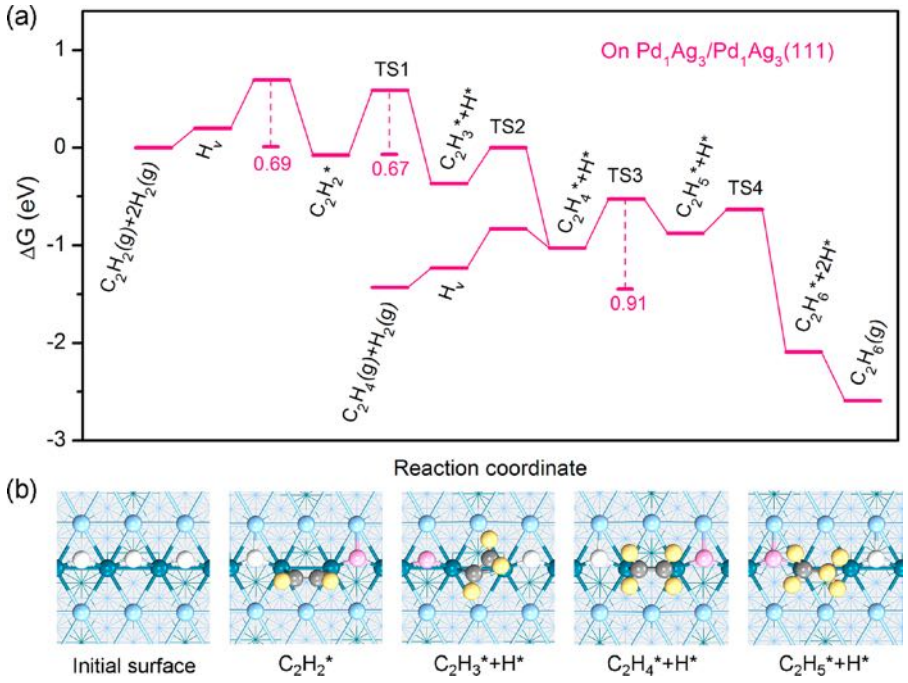

Figure 3. (a) Gibbs free energy profile for acetylene/ethene hydrogenation on $Pd_1Ag_3/Pd_1Ag_3(111)$, under the typical reaction conditions of 25 °C, $p(H_2)$ = 0.05 atm, $p(C_2H_2)$ = 0.005 atm, $p(C_2H_4)$ = 0.5 atm, and $p(C_2H_6)$ = 0.005 atm. (b) Structure snapshots for the reaction intermediates on $Pd_1Ag_3/Pd_1Ag_3(111)$. Color code: H atoms of hydrocarbon, yellow balls; H atoms reacting with hydrocarbons, pink balls; other H atoms, white balls; Pd atoms, indigo balls; Ag atoms, light blue balls; C atoms, gray balls.

Table 1. Adsorption Energy (E_{ad}), Adsorption Free Energy (G_{ad}), and Overall Hydrogenation Barrier (G_a) for Acetylene/Ethene Hydrogenation on the Low-Energy Surfaces of Pd_1Ag_3 ($Pm3m$) and Pd_1Ag_1 ($R3m$) with Different Surface Pd Ensembles[a]

			acetylene			ethene		
surface	Pd ensemble	initial H coverage (ML)	E_{ad} (eV)	G_{ad} (eV)	G_a (eV)	E_{ad} (eV)	G_{ad} (eV)	G_a (eV)
$Pd_1Ag_3/Pd_1Ag_3(111)$	Pd line	0.25	−0.73	−0.08	0.67	−0.18	0.41	0.91
$Pd_{11}Ag_5/Pd_1Ag_3(111)$	Pd_3	0.5	−1.11	−0.46	0.80	−0.11	0.48	1.29
$Pd/Pd_1Ag_3(111)$	Pd layer	1	−0.68	−0.03	0.74	0.00	0.59	1.38
$Pd_1Ag_7/Pd_1Ag_3(100)$	Pd_2	0.1875	−0.98	−0.33	0.67	−0.39	0.20	0.76
$Pd/Pd_1Ag_1(111)$	Pd layer	1	−0.67	−0.02	0.60	0.00	0.59	1.12
$Pd_3Ag_1/Pd_1Ag_1(100)$	Pd_5	1	−0.76	−0.11	0.78	−0.31	0.28	0.81

[a]The adsorption energy is with respect to the initial surface, while the free energy is with respect to the gas-phase acetylene, ethene, and hydrogen under the typical reaction conditions: i.e., 25 °C, $p(H_2)$ = 0.05 atm, $p(C_2H_2)$ = 0.005 atm, and $p(C_2H_4)$ = 0.5 atm.

dimer with H adsorbed at the bridge site, is already 0.024 eV less stable than the former.

For Pd_1Ag_1, the major difference in comparison to Pd_1Ag_3 is that the most stable surfaces always have Pd exposure, no matter whether the surface is (111) or (100). The most stable configurations, $Pd/Pd_1Ag_1(111)$-1 ML H (Pd layer ensemble) and $Pd_3Ag_1/Pd_1Ag_1(100)$-1 ML H (Pd_5 ensemble), both have surface H and the coverage is up to 1 ML with respect to the surface metal atom. Our results of Pd_1Ag_1 are summarized in Figure S2 in the Supporting Information, including the formation free energy contour maps and the lowest energy configurations.

The above thermodynamics analyses for the surface structures confirm the facts that Ag tends to segregate on the surfaces of PdAg alloys, but the adsorbates, i.e. H, can hinder the Ag segregation by forming Pd−H bonds on the surfaces. Importantly, our results indicate that under typical reductive reaction conditions with H adsorbates, only below Pd:Ag = 1:3 could the most stable surfaces ((111) and (100)) be fully covered by Ag. In addition, Ag segregation occurs preferentially on (100), while it is almost thermoneutral for the Pd exposure on $Pd_1Ag_3(111)$ in the presence of H_2.

3.3. Reaction Energy Profile. With the knowledge of PdAg surfaces, we then investigated the acetylene/ethene hydrogenation pathways on several representative surfaces with Pd exposure, including $Pd_1Ag_3/Pd_1Ag_3(111)$, $Pd_{11}Ag_5/Pd_1Ag_3(111)$, $Pd/Pd_1Ag_3(111)$, $Pd_1Ag_7/Pd_1Ag_3(100)$, $Pd/Pd_1Ag_1(111)$, and $Pd_3Ag_1/Pd_1Ag_1(100)$. It should be emphasized that the hydrogenation reaction could not occur on the Ag-covered surfaces due to the difficulty in H_2 dissociation and acetylene adsorption. However, on the Pd-exposed surfaces, the reaction mechanism for acetylene hydrogenation, as determined from SSW-NN based reaction pathway sampling,[43] is generally the same as that on the Pd surfaces reported previously:[20] namely, the Horiuti−Polanyi sequential hydrogenation via the intermediates of vinyl (C_2H_3), ethene, and ethyl (C_2H_5). As a representative, Figure 3a shows the Gibbs free energy profile for the lowest hydrogenation pathway on $Pd_1Ag_3/Pd_1Ag_3(111)$ under the typical reaction conditions: i.e., 25 °C, $p(H_2)$ = 0.05 atm, $p(C_2H_2)$ = 0.005 atm, $p(C_2H_4)$ = 0.5 atm, and $p(C_2H_6)$ =

https://doi.org/10.1021/jacs.1c02471
J. Am. Chem. Soc. 2021, 143, 6281−6292

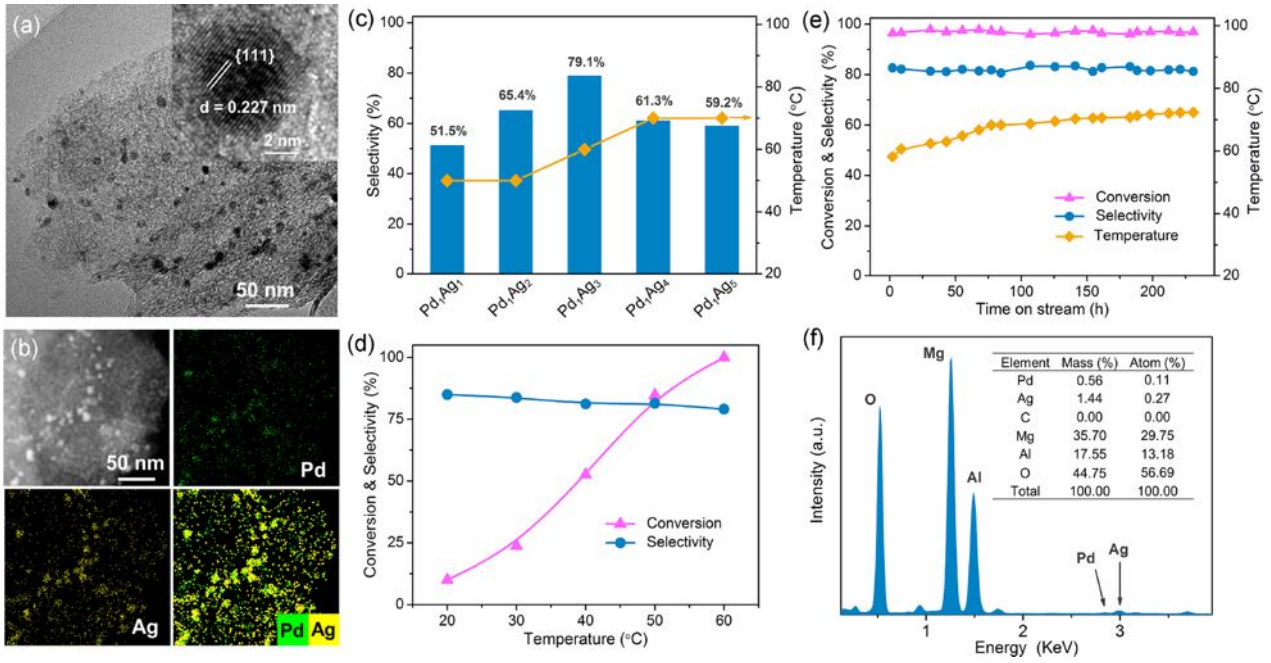

Figure 4. (a) TEM image of Pd_1Ag_3/HT and an enlarged view from the HR-TEM image (inset). (b) EDS elemental mapping image of Pd_1Ag_3/HT. (c) Selectivity and reaction temperature of the PdAg/HT catalysts with different Pd/Ag ratios at 100% acetylene conversion. (d) Conversion of acetylene and selectivity to ethene versus temperature on Pd_1Ag_3/HT. (e) Selectivity of Pd_1Ag_3/HT over 200 h at a high conversion of acetylene (>96%) as modulated by reaction temperature. (f) EDS pattern of Pd_1Ag_3/HT after a 200 h test.

0.005 atm. The key kinetic parameters of the reaction on $Pd_1Ag_3/Pd_1Ag_3(111)$ and the other surfaces are summarized in Table 1, including the adsorption energy, the adsorption free energy, and the overall free energy barrier.

On $Pd_1Ag_3/Pd_1Ag_3(111)$, the surface featuring Pd lines along ⟨110⟩ (see Figure 3b), the reaction starts from the acetylene adsorption at the Pd bridge site near to a surface hydrogen vacancy (H_v). The adsorption needs to overcome an overall barrier of 0.69 eV, for the creation of H_v (+0.20 eV) and the loss of translational and rotational entropy of the gas-phase acetylene (+0.49 eV). The adsorbed acetylene (see Figure 3b, C_2H_2*) is only 0.08 eV more stable in free energy with respect to the gas-phase acetylene and hydrogen. Next, the adsorbed acetylene can react with the nearby surface H atoms to give vinyl and ethene in a consecutive way, overcoming barriers of 0.67 and 0.37 eV, respectively. The process is exothermic, and thus the reverse reaction is inhibited kinetically. Meanwhile, the consumed surface H can be refilled quickly from the H_2 dissociation, which has a low barrier of 0.38 eV. Overall, both the acetylene adsorption and the first hydrogenation are rate-determining from acetylene to ethene, with close free energy barriers (0.69 and 0.67 eV).

Similarly, for ethene, it also prefers to adsorb at the available Pd bridge site near to H_v, which is however endothermic by 0.41 eV in free energy. Its hydrogenation to ethyl and to ethane needs to overcome barriers of 0.50 and 0.24 eV, respectively. Therefore, the rate-determining step is from ethene to ethyl with an overall barrier of 0.91 eV, which is significantly higher than the overall barrier from acetylene to ethene (0.69 eV). Due to the local high H coverage, the ethene desorption is facile with only a 0.2 eV barrier, which is much lower than its further hydrogenation barrier (0.50 eV).

As given in Table 1, for $Pd_{11}Ag_5/Pd_1Ag_3(111)$ and $Pd/Pd_1Ag_3(111)$, the other two representative (111) surfaces of Pd_1Ag_3 with the surface ensemble of Pd_3 and Pd layers (see the detailed PdAg patterns in Figure 2c), the acetylene hydrogenation barriers increase to 0.80 and 0.74 eV, respectively, while the ethene hydrogenation barriers increase to 1.29 and 1.38 eV, respectively, in comparison to those on $Pd_1Ag_3/Pd_1Ag_3(111)$. In contrast, on $Pd_1Ag_7/Pd_1Ag_3(100)$, the (100) surface of Pd_1Ag_3 with Pd dimer, the acetylene hydrogenation barrier is the same as that on $Pd_1Ag_3/Pd_1Ag_3(111)$, but the ethene hydrogenation barrier is much lower (only 0.76 eV). For $Pd/Pd_1Ag_1(111)$ and $Pd_3Ag_1/Pd_1Ag_1(100)$, the two surfaces of Pd_1Ag_1, the hydrogenation barriers are comparable to those on $Pd/Pd_1Ag_3(111)$ and $Pd_1Ag_7/Pd_1Ag_3(100)$.

From the data in Table 1, we can see that the hydrogenation of acetylene and ethene are complexly influenced by the PdAg bulk, the PdAg surface pattern, and the preadsorbed H, which suggests the significance of the thermodynamics phase diagrams for the PdAg bulk and surface (see Figures 1 and 2). Nevertheless, some general rules can be summarized as follows.

(i) $Pd_1Ag_1(111)$ has the lowest barrier (0.60 eV) for acetylene hydrogenation, but the barrier on $Pd_1Ag_3(111)$ is not much higher (0.67 eV).

(ii) (100) surfaces generally have poorer selectivity in comparison to (111) surfaces, as reflected by their close barriers for the hydrogenation of acetylene and ethene. In particular, $Pd_3Ag_1/Pd_1Ag_1(100)$ has the worst selectivity, with the hydrogenation barrier of ethene being only slightly higher (0.03 eV) than that of acetylene.

(iii) The activity is sensitive to the local PdAg patterns. For Pd_1Ag_3, the Pd_2 and Pd line local patterns appear to be more active with lower acetylene hydrogenation barriers in comparison to the Pd_3 and Pd layer patterns.

We have performed electronic structure analysis on the PdAg surfaces. No clear correlation between the electronic structure and the reaction barrier can be obtained. For example, Figure S3 shows the Pd d states for $Pd/Pd_1Ag_3(111)$ and $Pd_3Ag_1/$

https://doi.org/10.1021/jacs.1c02471
J. Am. Chem. Soc. 2021, 143, 6281−6292

$Pd_1Ag_1(100)$, which have quite close d band centers for the surface Pd (−2.53 and −2.42 eV). However, their ethene hydrogenation barriers are vastly different (1.38 and 0.81 eV).

It is of interest to compare our results with previous DFT calculations. We note that most of the previous works typically utilized models constructed by a manually configurated PdAg layer on the Pd bulk due to the lack of global PES exploration and the lack of the consideration of realistic H coverage under the reaction conditions. It is therefore not surprising that their reported energetics are quite different from the results in this work.[1,35,37] For example, Smith et al.[35] have calculated the hydrogenation reactions on clean $Pd_1Ag_1/Pd(111)$ with no precovered H and obtained adsorption energies of −1.31 and −0.73 eV for acetylene and ethene, respectively, which are much higher than our results on $Pd_1Ag_3/Pd_1Ag_3(111)$, −0.73 and −0.18 eV (−0.08 and 0.41 eV in free energy). In addition, their results for the acetylene and ethene hydrogenation barriers are 0.69 and 0.63 eV,[37] respectively, where the ethene hydrogenation barrier is significantly lower than our result (0.91 eV) on $Pd_1Ag_3/Pd_1Ag_3(111)$. A recent study by Xie et al.[64] reported that the ethene desorption barrier on Pd(111) at the low H coverage and high C_2H_2 coverage (corresponding to low conversion rate) is 0.51 eV at 300 K. This reaction condition as reflected by the surface coverage is different from the high conversion condition (high H_2 pressure) here, where ethene desorption is no longer a problem and the selectivity is mostly determined by the hydrogenation barrier difference between acetylene and ethene. With these comparisons, we again emphasize the influence of PdAg bulk, PdAg surface pattern, and the preadsorbed H on the hydrogenation kinetics.

3.4. Catalytic Hydrogenation Experiment. Since theory discovers many likely PdAg patterns on PdAg alloy surfaces, which have different hydrogenation kinetics, it is intriguing to ask whether these patterns exist in real catalysts and how they affect the catalytic performance. To this end, we have first synthesized a series of HT (MgAl hydrotalcite)-supported PdAg nanoparticles with different Pd/Ag ratios, including Pd, Pd_1Ag_1, Pd_1Ag_2, Pd_1Ag_3, Pd_1Ag_4, and Pd_1Ag_5, to examine their catalytic performance. These catalysts have been characterized by X-ray diffraction (XRD), transmission electron microscopy (TEM), and energy dispersive X-ray spectroscopy elemental mapping (EDS mapping), as detailed in Figures S4−S6 in the Supporting Information. Figure 4a shows a representative TEM picture for the synthesized Pd_1Ag_3/HT catalyst, where the PdAg nanoparticles are uniformly dispersed on the HT support with an average particle size of 6.4 nm. The distance between the close-packed (111) planes is 0.227 nm for the nanoparticles, which is between that of fcc Pd (0.224 nm) and fcc Ag (0.236 nm)[65] and is consistent with the theoretically predicted values (0.236, 0.228, and 0.240 nm for Pd_1Ag_3, Pd, and Ag from DFT calculations with the PBE functional). The EDS mapping in Figure 4b confirms the formation of PdAg alloy with nice spatial overlap between Pd and Ag. In line with the theoretical convex hull diagram (see Figure 1a), our XRD data (as provided in Figure S4 in the Supporting Information) confirms the formation of new PdAg crystal phases at Pd_1Ag_1 and Pd_1Ag_3, which show new peaks at 39.6 and 39.1°, respectively, in comparison with the peaks at 40.0° for Pd and 38.1° for Ag. No new peaks have been identified for the samples Pd_1Ag_2, Pd_1Ag_4, and Pd_1Ag_5.

Our acetylene hydrogenation experiments were then carried out in a continuous-flow fixed-bed microreactor with the feed gas consisting of 0.5% C_2H_2, 50.0% C_2H_4, 5.0% H_2, 4.0% He, and 40.5% N_2 at a space velocity of 96000 mL/(g h). The catalytic data were typically collected at the steady state: i.e., after 1 h in stream. We found that all of the PdAg catalysts can efficiently convert acetylene to ethene or ethane at low temperatures (below 100 °C). To compare their selectivity, we kept the 100% acetylene conversion by varying the reaction temperature, and the results for all the catalysts are shown in Figure 4c. It is clear that Pd_1Ag_3 achieves the highest selectivity of 79.1%, while Pd_1Ag_1 has the lowest performance (51.5%). From Pd_1Ag_1 to Pd_1Ag_3, with an increase in Ag content, the selectivity increases from 51.5% to 79.1%, and then from Pd_1Ag_3 to Pd_1Ag_5, the selectivity drops gradually to 59.2%. These results demonstrate that the Ag content is critical to the selectivity.

Figure 4d shows the temperature dependence for the activity and selectivity of Pd_1Ag_3. The acetylene conversion increases from 10% to 100% with reaction temperatures from 20 to 60 °C, while the selectivity maintains quite steady at around 80%. This implies that there are a set of different active sites on the Pd_1Ag_3 catalyst: i.e., both the sites with good selectivity and those with poor selectivity, and the concentration of the sites do not change significantly in a short amount of time with respect to the reaction temperature.

In order to reveal whether the catalyst does undergo structural evolution during the hydrogenation, we have performed a long-term catalyst test. Figure 4e shows the selectivity and reaction temperature for Pd_1Ag_3/HT over a 200 h reaction at a high acetylene conversion of >96%, which was maintained by monitoring and modulating the temperature. We found that the selectivity can be maintained above 80% throughout the 200 h reaction time and the reaction temperature increases gradually from 58 to 72 °C. After the 200 h test, the catalyst was analyzed by HR-TEM (Figure S7 in the Supporting Information) and the EDS pattern (Figure 4f), which show nearly no change in the particle size and no detectable deposition of carbon on the catalyst. The sintering of the nanoparticles and the formation of high-carbon-weight overlayers that block the catalyst sites can thus be ruled out. Instead, the increase in reaction temperature to maintain high conversion is a solid indication of the internal structural evolution of PdAg nanoparticles, where the newly emerging sites have lower activity but keep a similar selectivity.

3.5. Microkinetic Simulation. To better understand the catalytic selectivity and surface structural evolution for the PdAg/HT catalysts, we have performed microkinetic simulations on three situations according to our surface thermodynamics phase diagrams (see Figure 2): the first is the Pd line ensemble on (111) ($Pd_1Ag_3/Pd_1Ag_3(111)$ surface) and the pure Ag covering (100), which corresponds to the thermodynamically favored configuration right after catalyst preparation, the second is the Pd layer on (111) ($Pd/Pd_1Ag_3(111)$ surface) and also the Pd dimer on (100) ($Pd_1Ag_7/Pd_1Ag_3(100)$ surface) at (111):(100) = 60:1, which mimics the likely more Pd exposed situation after the long-term catalytic reaction, and the third is based on the Pd_1Ag_1 catalyst, including the Pd layer on (111) ($Pd/Pd_1Ag_1(111)$ surface) and Pd_5 ensemble on (100) ($Pd_3Ag_1/Pd_1Ag_1(100)$ surface) at (111):(100) = 10:1, which corresponds to the favored Pd_1Ag_1 surfaces.

A continuously stirred tank model was built up to simulate the reactions in the fixed bed reactor: i.e., the feed gas inflows a tank while the reacted gas outflows in every time interval. According to our experimental conditions, the simulations have the following setup: the feed gas consists of H_2, C_2H_2, and C_2H_4 in the ratio of 5:0.5:50, the contact time is set to be 0.01 s, i.e. in every 10^{-6} s, we add 0.01% feed gas into the tank and remove

https://doi.org/10.1021/jacs.1c02471
J. Am. Chem. Soc. 2021, 143, 6281−6292

0.01% reacted gas, and the reactions take place at 60 °C. The kinetic parameters based on the hydrogenation energetics (see Figure 3 and Table 1) are summarized in Table S3 in the Supporting Information.

Figure 5 shows the time-resolved contents of acetylene, increased ethene, and ethane from the simulations. For the reaction on $Pd_1Ag_3/Pd_1Ag_3(111)$ (see Figure 5a), the acetylene content is quickly consumed from 1 to 0.04 within 1.5×10^{-3} s due to the adsorption and hydrogenation on the surface and then remains nearly constant, leading to a conversion of 96.3%. Meanwhile, ethene is generated from the hydrogenation of acetylene and reaches a maximum content of 0.935 at 2.5×10^{-3} s, which then slightly drops to 0.87 at 2×10^{-2} s due to the further hydrogenation to ethane. Of interest, the times for acetylene adsorption (1.5×10^{-3} s) and hydrogenation (2.5×10^{-3} s) are comparable, resulting from their similar barriers (0.69 and 0.67 eV). The final selectivity to ethene is 90.5%.

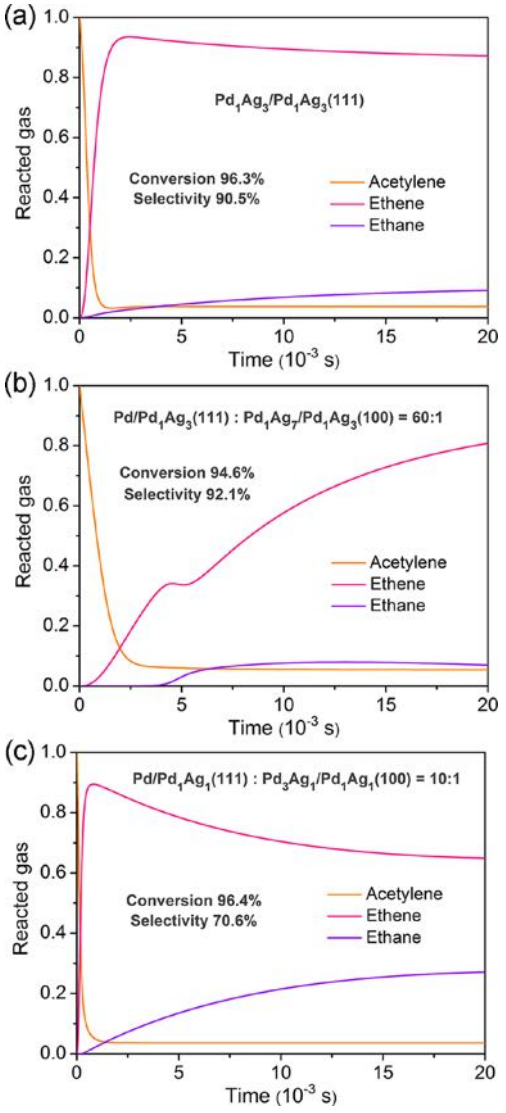

Figure 5. Time-resolved reaction curve from microkinetic simulations at 60 °C and $p(H_2):p(C_2H_2):p(C_2H_4)$ = 5:0.5:50 for (a) $Pd_1Ag_3/Pd_1Ag_3(111)$, (b) $Pd/Pd_1Ag_3(111):Pd_1Ag_7/Pd_1Ag_3(100)$ = 60:1, and (c) $Pd/Pd_1Ag_1(111):Pd_3Ag_1/Pd_1Ag_1(100)$ = 10:1.

In contrast, for the reaction on $Pd/Pd_1Ag_3(111)$ and $Pd_1Ag_7/Pd_1Ag_3(100)$ with the catalytic sites at a ratio of 60:1 (see Figure 5b), the time for acetylene adsorption (2.5×10^{-3} s) is comparable to that on $Pd_1Ag_3/Pd_1Ag_3(111)$ (1.5×10^{-3} s), but the acetylene hydrogenation to ethene becomes much slower (2×10^{-2} s), which is the result of the increased hydrogenation barrier (0.74 eV). This reduces the acetylene conversion to 94.6%. Importantly, since there is a minor presence of Pd dimer sites exposed on (100), which provide a relatively low energy pathway for the deep hydrogenation (0.76 eV), ethane is generated at 5×10^{-3} s, leading to a small turning point for the increase in ethene product. The final selectivity is 92.1%, benefitting from the high ethene hydrogenation barrier (1.38 eV) on $Pd/Pd_1Ag_3(111)$.

For Pd_1Ag_1 (Figure 5c), we found that the acetylene consumption and the conversion (96.4%) are nearly the same as that on $Pd_1Ag_3/Pd_1Ag_3(111)$, which is limited by the acetylene adsorption step (0.69 eV). However, due to the appreciable presence of (111):(100) = 10:1 and the favorable Pd exposure on (100), the catalyst can also hydrogenate ethene, which leads to a final selectivity of only 70.7%, much lower than that on $Pd_1Ag_3/Pd_1Ag_3(111)$.

On the basis of the results from microkinetic simulations, we are now in a position to discuss the observed conversion and selectivity of the PdAg catalysts in experiment. For Pd_1Ag_3, we confirm in microkinetics that the Pd layer ensemble, with an acetylene hydrogenation barrier of 0.74 eV, is indeed less active than the Pd line ensemble (0.67 eV) and the reaction temperature needs to increase to maintain the acetylene conversion. This completes the reaction picture that Pd atoms gradually accumulate onto the surface layer over the long-term experiment accompanied by a decrease in activity. The selectivity of the catalyst is well maintained due to the major Ag coverage on the (100) surface: the population of Pd on (111) improves the selectivity but has the reverse effect on (100), which cancels each other in the overall effect. In contrast, for Pd_1Ag_1, the selectivity is much lower due to the high exposure of Pd atoms on (100).

4. CATALYST SCREENING AND DISCUSSION

The combination of theory and experiment allows us to provide deeper insights into the PdAg catalyst. Pd_1Ag_3 is the best Pd:Ag ratio, where Pd atoms are maximally separated from each other and (100) can be mostly terminated by Ag; there is a tendency for Pd to aggregate onto the surface over a long reaction time, which may dramatically reduce the selectivity if Pd_1Ag_1 is locally present. The (100) surface is generally undesirable, which is the cause for the low selectivity. This key information has inspired us to search for a better PdAg catalyst by controlling the Pd:Ag ratio and search for a support to finely disperse PdAg and to better terminate the (100) surface. The finely dispersed PdAg will reduce the area of (111) and (100), which thus limits the PdAg local surface patterns and decreases the possibility of the inhomogeneous presence of Pd_1Ag_1 in Pd_1Ag_3.

For this purpose, a series of common support materials, including α-Al_2O_3, γ-Al_2O_3, SiO_2, Y_2O_3, $CaCO_3$, rutile-TiO_2 (r-TiO_2), anatase-TiO_2 (a-TiO_2), P25, and Ti-MWW, have been tested for the synthesis of the Pd_1Ag_3 catalyst. These catalysts were then tested for the catalytic performance, and the results are shown in Figure 6a, which compares the catalytic selectivity at 100% acetylene conversion. We found that Pd_1Ag_3/rutile-TiO_2 is the best catalyst, even overperforming Pd_1Ag_3/HT. Interestingly, the change in TiO_2 phase from rutile to anatase will significantly reduce the selectivity, and a mixture of rutile and anatase phases, i.e. the P25 material, also gives lower

https://doi.org/10.1021/jacs.1c02471
J. Am. Chem. Soc. 2021, 143, 6281−6292

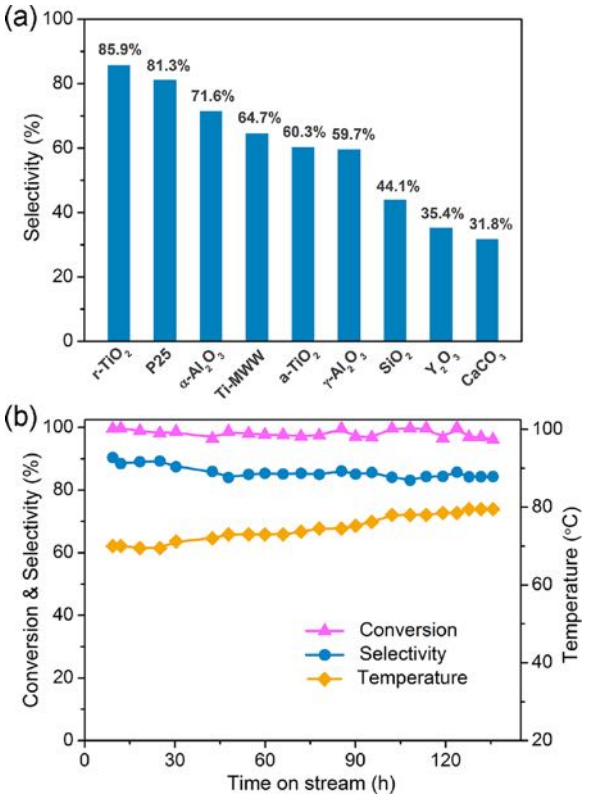

Figure 6. (a) Selectivity of Pd_1Ag_3 catalysts on different supports at 100% acetylene conversion. (b) Selectivity of Pd_1Ag_3/rutile-TiO_2 over 100 h at a high conversion of acetylene (>96%) as modulated by the reaction temperature.

selectivity in comparison to the pure rutile phase. Our HR-TEM and XRD data (Figures S8 and S9 in the Supporting Information) for Pd_1Ag_3/rutile-TiO_2 indicate that the rutile support can finely disperse the Pd_1Ag_3 nanoparticles with an average size of below 4.9 nm, which is ∼2 nm smaller than that on Pd_1Ag_3/HT. In the sample, there is no obvious peak for an fcc crystal from XRD, and the large PdAg crystalline particles are also much more scarce in comparison to those on the HT support, as shown by HR-TEM. Indeed, our ongoing SSW-NN simulations found that small Pd_1Ag_3 nanoparticles (N_{atom} < 50) on rutile-TiO_2(110) prefer to expose (111)-like facets with an exposed Pd_2 local structure (see Figure S10 in the Supporting Information), which could be the key to the high selectivity of the catalyst.

A long-term catalyst test for Pd_1Ag_3/rutile-TiO_2 was also performed to examine the catalyst stability, and the results are shown in Figure 6b. We found that the Pd_1Ag_3/rutile-TiO_2 catalyst can maintain a good selectivity above 85% at a conversion of >96% over the 100 h catalyst test. Similarly, the reaction temperature increases slightly from 70 to 80 °C during the catalyst test at the constant high conversion rate.

Finally, we discuss the performance of Pd_1Ag_3/rutile-TiO_2 in the context of previously reported catalysts (also see the detailed catalyst summary for acetylene hydrogenation in Table S5 in the Supporting Information). We note that the previous low-temperature catalysts for acetylene selective hydrogenation generally adopt the Pd element as the active component. This is because the replacement of Pd by Ni or Fe elements will elevate the reaction temperature up to 200 °C,[4,10,66−68] which is undesirable in industry due to the need to heat up the feed gas.[7−9] Therefore, we mainly focus on the comparison within Pd-based catalysts. Armbrüster et al.[21,22,69,70] have shown that, in addition to PdAg, the PdGa alloy can also improve the selectivity of pure Pd, and the Pd_2Ga_1/Al_2O_3 catalyst achieves the best selectivity of 75% at a high acetylene conversion (>95%). The Pd-In alloy is also likely to be a good candidate: Feng et al.[24] achieved a high selectivity of 92% on $Pd_1In_1/MgAl_2O_4$ catalyst, but Cao et al.[25] obtained a much lower selectivity of 77% on Pd_1In_1/Al_2O_3. We thus conclude that the Pd_1Ag_3/rutile-TiO_2 catalyst identified in this work is indeed among the catalysts with a top-level performance (conversion >96%, selectivity >85%).

5. CONCLUSIONS

By a combination of machine-learning atomic simulation and experiment, this work revealed the catalytic role of Ag in PdAg-catalyzed acetylene selective hydrogenation and identified a rutile-supported Pd_1Ag_3 catalyst with good performance at low temperatures. The advent of global neural network potential techniques allowed us to quickly assess millions of structure candidates for complex catalyst structures, which led to the resolution of the bulk and surface phase diagrams of Pd-Ag-H. The combination of catalysis experiments and microkinetic simulations based on low-energy pathway energetics provided a consistent explanation of the dynamic catalyst evolution during catalytic conversion. This combinatory approach opens the door for the rational design of complex catalyst systems in the future. The key findings of this work are further outlined below.

(i) The formation energies of PdAg alloys are generally small (below −0.06 eV/atom), but the presence of Ag inhibits the dissolution of H in the PdAg bulk. Two typical bulk structures, Pd_1Ag_1 ($R\bar{3}m$) and Pd_1Ag_3 ($Pm\bar{3}m$) have been identified. In Pd_1Ag_3, Pd atoms can be maximally separated with Pd being in the second-neighbor shell of Pd.

(ii) Ag tends to segregate on the surfaces of PdAg alloys, but H adsorption can reverse the process, which can produce a range of surface patterns, including the Pd line, Pd_2, Pd_3, Pd_5, and Pd layer ensembles on the surface. In particular, Ag prefers to segregate on (100) and under typical reaction conditions (i.e., 25 °C, $p(H_2)$ = 0.05 atm) Pd is no longer favorably exposed on (100) when Pd/Ag ≤ 1/3.

(iii) For acetylene hydrogenation, the (111) surfaces are generally more selective than the (100) surfaces. Pd_1Ag_3, with (100) being entirely covered by Ag, can achieve the best catalytic performance (>90% selectivity in theory).

(iv) It is evident that Pd atoms slowly accumulate onto the surface layer during catalytic conversion. This Pd surface segregation reduces the activity due to the formation of Pd_3 and Pd layer ensembles, which have higher ethene hydrogenation barriers (0.80 and 0.74 eV) in comparison to the Pd line ensemble (0.67 eV). To keep the same activity, the reaction temperature needs to be increased slightly.

(v) A rutile-supported Pd_1Ag_3 catalyst is identified to achieve the best catalytic performance (conversion >96%, selectivity >85%) over a long-term catalysis test.

■ ASSOCIATED CONTENT

Supporting Information

The Supporting Information is available free of charge at https://pubs.acs.org/doi/10.1021/jacs.1c02471.

https://doi.org/10.1021/jacs.1c02471
J. Am. Chem. Soc. 2021, 143, 6281−6292

Theoretical methodology and the construction of the quaternary Pd-Ag--H G-NN potential, surface structures of Pd_1Ag_1, electronic structures of $Pd/Pd_1Ag_3(111)$ and $Pd_3Ag_1/Pd_1Ag_1(100)$, kinetic parameters utilized in microkinetic simulations, preliminary results for PdAg nanoparticles on TiO_2, and experimental details of the synthesis and characterization of different acetylene hydrogenation catalysts (PDF)

XYZ coordinates for the key structure configurations in Figure 3 (XYZ)

AUTHOR INFORMATION

Corresponding Author

Zhi-Pan Liu − *Collaborative Innovation Center of Chemistry for Energy Material, Shanghai Key Laboratory of Molecular Catalysis and Innovative Materials, Key Laboratory of Computational Physical Science, Department of Chemistry, Fudan University, Shanghai 200433, China;* orcid.org/0000-0002-2906-5217; Email: zpliu@fudan.edu.cn

Authors

Xiao-Tian Li − *Collaborative Innovation Center of Chemistry for Energy Material, Shanghai Key Laboratory of Molecular Catalysis and Innovative Materials, Key Laboratory of Computational Physical Science, Department of Chemistry, Fudan University, Shanghai 200433, China*

Lin Chen − *Collaborative Innovation Center of Chemistry for Energy Material, Shanghai Key Laboratory of Molecular Catalysis and Innovative Materials, Key Laboratory of Computational Physical Science, Department of Chemistry, Fudan University, Shanghai 200433, China;* orcid.org/0000-0002-7145-7564

Cheng Shang − *Collaborative Innovation Center of Chemistry for Energy Material, Shanghai Key Laboratory of Molecular Catalysis and Innovative Materials, Key Laboratory of Computational Physical Science, Department of Chemistry, Fudan University, Shanghai 200433, China;* orcid.org/0000-0001-7486-1514

Complete contact information is available at: https://pubs.acs.org/10.1021/jacs.1c02471

Author Contributions

†X.-T.L. and L.C. contributed equally to this work.

Notes

The authors declare no competing financial interest.

ACKNOWLEDGMENTS

This work was supported by the National Key Research and Development Program of China (2018YFA0208600) and the National Science Foundation of China (22033003, 21533001, and 91745201).

REFERENCES

(1) Studt, F.; Abild-Pedersen, F.; Bligaard, T.; Sørensen, R. Z.; Christensen, C. H.; Nørskov, J. K. Identification of Non-Precious Metal Alloy Catalysts for Selective Hydrogenation of Acetylene. *Science* **2008**, *320*, 1320−1322.

(2) Teschner, D.; Borsodi, J.; Wootsch, A.; Révay, Z.; Hävecker, M.; Knop-Gericke, A.; Jackson, S. D.; Schlögl, R. The Roles of Subsurface Carbon and Hydrogen in Palladium-Catalyzed Alkyne Hydrogenation. *Science* **2008**, *320*, 86−89.

(3) Kyriakou, G.; Boucher, M.; Jewell, A.; Lewis, E.; Lawton, T.; Baber, A.; Tierney, H.; Flytzani-Stephanopoulos, M.; Sykes, C. Isolated Metal Atom Geometries as a Strategy for Selective Heterogeneous Hydrogenations. *Science* **2012**, *335*, 1209−1212.

(4) Armbrüster, M.; Kovnir, K.; Friedrich, M.; Teschner, D.; Wowsnick, G.; Hahne, M.; Gille, P.; Szentmiklósi, L.; Feuerbacher, M.; Heggen, M.; Girgsdies, F.; Rosenthal, D.; Schlögl, R.; Grin, Y. Al13Fe4 as a Low-Cost Alternative for Palladium in Heterogeneous Hydrogenation. *Nat. Mater.* **2012**, *11*, 690−693.

(5) Wei, S.; Li, A.; Liu, J.; Li, Z.; Chen, W.; Gong, Y.; Zhang, Q.; Cheong, W.-C. M.; Wang, Y.; Zheng, L.; Xiao, H.; Chen, C.; Wang, D.; Peng, Q.; Gu, L.; Han, X.; Li, J.; Li, Y. Direct Observation of Noble Metal Nanoparticles Transforming to Thermally Stable Single Atoms. *Nat. Nanotechnol.* **2018**, *13*, 856−861.

(6) Zhang, L.; Zhou, M.; Wang, A.; Zhang, T. Selective Hydrogenation over Supported Metal Catalysts: From Nanoparticles to Single Atoms. *Chem. Rev.* **2020**, *120*, 683−733.

(7) Borodziński, A.; Bond, G. C. Selective Hydrogenation of Ethyne in Ethene-Rich Streams on Palladium Catalysts. Part 1. Effect of Changes to the Catalyst During Reaction. *Catal. Rev.: Sci. Eng.* **2006**, *48*, 91−144.

(8) Borodziński, A.; Bond, G. C. Selective Hydrogenation of Ethyne in Ethene-Rich Streams on Palladium Catalysts, Part 2: Steady-State Kinetics and Effects of Palladium Particle Size, Carbon Monoxide, and Promoters. *Catal. Rev.: Sci. Eng.* **2008**, *50*, 379−469.

(9) McCue, A. J.; Anderson, J. A. Recent Advances in Selective Acetylene Hydrogenation Using Palladium Containing Catalysts. *Front. Chem. Sci. Eng.* **2015**, *9*, 142−153.

(10) Liu, Y.; Liu, X.; Feng, Q.; He, D.; Zhang, L.; Lian, C.; Shen, R.; Zhao, G.; Ji, Y.; Wang, D.; Zhou, G.; Li, Y. Intermetallic. Nix My (M = Ga and Sn) Nanocrystals: A Non-Precious Metal Catalyst for Semi-Hydrogenation of Alkynes. *Adv. Mater.* **2016**, *28*, 4747−4754.

(11) Zhang, Q.; Li, J.; Liu, X.; Zhu, Q. Synergetic Effect of Pd and Ag Dispersed on Al2O3 in the Selective Hydrogenation of Acetylene. *Appl. Catal., A* **2000**, *197*, 221−228.

(12) Zea, H.; Lester, K.; Datye, A. K.; Rightor, E.; Gulotty, R.; Waterman, W.; Smith, M. The Influence of Pd−Ag Catalyst Restructuring on the Activation Energy for Ethylene Hydrogenation in Ethylene−Acetylene Mixtures. *Appl. Catal., A* **2005**, *282*, 237−245.

(13) Khan, N. A.; Shaikhutdinov, S.; Freund, H. J. Acetylene and Ethylene Hydrogenation on Alumina Supported Pd-Ag Model Catalysts. *Catal. Lett.* **2006**, *108*, 159−164.

(14) Lee, J. H.; Kim, S. K.; Ahn, I. Y.; Kim, W.-J.; Moon, S. H. Performance of Pd−Ag/Al2O3 Catalysts Prepared by the Selective Deposition of Ag onto Pd in Acetylene Hydrogenation. *Catal. Commun.* **2011**, *12*, 1251−1254.

(15) Han, Y.; Peng, D.; Xu, Z.; Wan, H.; Zheng, S.; Zhu, D. TiO2 Supported Pd@Ag as Highly Selective Catalysts for Hydrogenation of Acetylene in Excess Ethylene. *Chem. Commun.* **2013**, *49*, 8350−8352.

(16) Ball, M. R.; Rivera-Dones, K. R.; Gilcher, E. B.; Ausman, S. F.; Hullfish, C. W.; Lebrón, E. A.; Dumesic, J. A. AgPd and CuPd Catalysts for Selective Hydrogenation of Acetylene. *ACS Catal.* **2020**, *10*, 8567−8581.

(17) Doyle, A. M.; Shaikhutdinov, S. K.; Jackson, S. D.; Freund, H.-J. Hydrogenation on Metal Surfaces: Why Are Nanoparticles More Active than Single Crystal. *Angew. Chem., Int. Ed.* **2003**, *42*, 5240−5243.

(18) Teschner, D.; Révay, Z.; Borsodi, J.; Hävecker, M.; Knop-Gericke, A.; Schlögl, R.; Milroy, D.; Jackson, S. D.; Torres, D.; Sautet, P. Understanding Palladium Hydrogenation Catalysts: When the Nature of the Reactive Molecule Controls the Nature of the Catalyst Active Phase. *Angew. Chem., Int. Ed.* **2008**, *47*, 9274−9278.

(19) Wilde, M.; Fukutani, K.; Ludwig, W.; Brandt, B.; Fischer, J.-H.; Schauermann, S.; Freund, H.-J. Influence of Carbon Deposition on the Hydrogen Distribution in Pd Nanoparticles and Their Reactivity in Olefin Hydrogenation. *Angew. Chem., Int. Ed.* **2008**, *47*, 9289−9293.

(20) Li, X.-T.; Chen, L.; Wei, G.-F.; Shang, C.; Liu, Z.-P. Sharp Increase in Catalytic Selectivity in Acetylene Semihydrogenation on Pd Achieved by a Machine Learning Simulation-Guided Experiment. *ACS Catal.* **2020**, *10*, 9694−9705.

(21) Armbrüster, M.; Kovnir, K.; Behrens, M.; Teschner, D.; Grin, Y.; Schlögl, R. Pd−Ga Intermetallic Compounds as Highly Selective

Semihydrogenation Catalysts. *J. Am. Chem. Soc.* **2010**, *132*, 14745−14747.
(22) Armbrüster, M.; Wowsnick, G.; Friedrich, M.; Heggen, M.; Cardoso-Gil, R. Synthesis and Catalytic Properties of Nanoparticulate Intermetallic Ga−Pd Compounds. *J. Am. Chem. Soc.* **2011**, *133*, 9112−9118.
(23) Shao, L.; Zhang, W.; Armbrüster, M.; Teschner, D.; Girgsdies, F.; Zhang, B.; Timpe, O.; Friedrich, M.; Schlögl, R.; Su, D. Nanosizing Intermetallic Compounds onto Carbon Nanotubes: Active and Selective Hydrogenation Catalysts. *Angew. Chem., Int. Ed.* **2011**, *50*, 10231−10235.
(24) Feng, Q.; Zhao, S.; Wang, Y.; Dong, J.; Chen, W.; He, D.; Wang, D.; Yang, J.; Zhu, Y.; Zhu, H.; Gu, L.; Li, Z.; Liu, Y.; Yu, R.; Li, J.; Li, Y. Isolated Single-Atom Pd Sites in Intermetallic Nanostructures: High Catalytic Selectivity for Semihydrogenation of Alkynes. *J. Am. Chem. Soc.* **2017**, *139*, 7294−7301.
(25) Cao, Y.; Sui, Z.; Zhu, Y.; Zhou, X.; Chen, D. Selective Hydrogenation of Acetylene over Pd-In/Al2O3 Catalyst: Promotional Effect of Indium and Composition-Dependent Performance. *ACS Catal.* **2017**, *7*, 7835−7846.
(26) Zhou, H.; Yang, X.; Li, L.; Liu, X.; Huang, Y.; Pan, X.; Wang, A.; Li, J.; Zhang, T. PdZn Intermetallic Nanostructure with Pd−Zn−Pd Ensembles for Highly Active and Chemoselective Semi-Hydrogenation of Acetylene. *ACS Catal.* **2016**, *6*, 1054−1061.
(27) Hu, M.; Zhao, S.; Liu, S.; Chen, C.; Chen, W.; Zhu, W.; Liang, C.; Cheong, W.-C.; Wang, Y.; Yu, Y.; Peng, Q.; Zhou, K.; Li, J.; Li, Y. MOF-Confined Sub-2 nm Atomically Ordered Intermetallic PdZn Nanoparticles as High-Performance Catalysts for Selective Hydrogenation of Acetylene. *Adv. Mater.* **2018**, *30*, 1801878.
(28) Karakaya, I.; Thompson, W. T. The Ag-Pd (Silver-Palladium) System. *Bull. Alloy Phase Diagrams* **1988**, *9*, 237−243.
(29) Müller, S.; Zunger, A. First-Principles Predictions of Yet-Unobserved Ordered Structures in the Ag-Pd Phase Diagram. *Phys. Rev. Lett.* **2001**, *87*, 165502.
(30) Wouda, P. T.; Schmid, M.; Nieuwenhuys, B. E.; Varga, P. STM Study of the (111) and (100) Surfaces of PdAg. *Surf. Sci.* **1998**, *417*, 292−300.
(31) Ruban, A. V.; Skriver, H. L.; Nørskov, J. K. Surface Segregation Energies in Transition-Metal Alloys. *Phys. Rev. B: Condens. Matter Mater. Phys.* **1999**, *59*, 15990−16000.
(32) Løvvik, O. M. Surface Segregation in Palladium Based Alloys from Density-Functional Calculations. *Surf. Sci.* **2005**, *583*, 100−106.
(33) Lim, J. S.; Vandermause, J.; van Spronsen, M. A.; Musaelian, A.; Xie, Y.; Sun, L.; O'Connor, C. R.; Egle, T.; Molinari, N.; Florian, J.; Duanmu, K.; Madix, R. J.; Sautet, P.; Friend, C. M.; Kozinsky, B. Evolution of Metastable Structures at Bimetallic Surfaces from Microscopy and Machine-Learning Molecular Dynamics. *J. Am. Chem. Soc.* **2020**, *142*, 15907−15916.
(34) Greeley, J.; Mavrikakis, M. Alloy Catalysts Designed from First Principles. *Nat. Mater.* **2004**, *3*, 810−815.
(35) Sheth, P. A.; Neurock, M.; Smith, C. M. First-Principles Analysis of the Effects of Alloying Pd with Ag for the Catalytic Hydrogenation of Acetylene−Ethylene Mixtures. *J. Phys. Chem. B* **2005**, *109*, 12449−12466.
(36) Studt, F.; Abild-Pedersen, F.; Bligaard, T.; Sørensen, R. Z.; Christensen, C. H.; Nørskov, J. K. On the Role of Surface Modifications of Palladium Catalysts in the Selective Hydrogenation of Acetylene. *Angew. Chem., Int. Ed.* **2008**, *47*, 9299−9302.
(37) Mei, D.; Neurock, M.; Smith, C. M. Hydrogenation of Acetylene−Ethylene Mixtures over Pd and Pd-Ag Alloys: First-Principles-Based Kinetic Monte Carlo Simulations. *J. Catal.* **2009**, *268*, 181−195.
(38) Tiruppathi, P.; Low, J. J.; Chan, A. S. Y.; Bare, S. R.; Meyer, R. J. Density Functional Theory Study of the Effect of Subsurface H, C, and Ag on C2H2 Hydrogenation on Pd(111). *Catal. Today* **2011**, *165*, 106−111.
(39) López, N.; Vargas-Fuentes, C. Promoters in the Hydrogenation of Alkynes in Mixtures: Insights from Density Functional Theory. *Chem. Commun.* **2012**, *48*, 1379−1391.
(40) Jørgensen, M.; Grönbeck, H. Selective Acetylene Hydrogenation over Single-Atom Alloy Nanoparticles by Kinetic Monte Carlo. *J. Am. Chem. Soc.* **2019**, *141*, 8541−8549.
(41) Huang, S.-D.; Shang, C.; Kang, P.-L.; Zhang, X.-J.; Liu, Z.-P. LASP: Fast Global Potential Energy Surface Exploration. *Wiley Interdiscip. Rev.: Comput. Mol. Sci.* **2019**, *9*, e1415.
(42) Ma, S.; Huang, S.-D.; Liu, Z.-P. Dynamic Coordination of Cations and Catalytic Selectivity on Zinc−Chromium Oxide Alloys during Syngas Conversion. *Nat. Catal.* **2019**, *2*, 671−677.
(43) Kang, P.-L.; Shang, C.; Liu, Z.-P. Glucose to 5-Hydroxymethylfurfural: Origin of Site-Selectivity Resolved by Machine Learning Based Reaction Sampling. *J. Am. Chem. Soc.* **2019**, *141*, 20525−20536.
(44) Kang, P.-L.; Shang, C.; Liu, Z.-P. Large-Scale Atomic Simulation via Machine Learning Potentials Constructed by Global Potential Energy Surface Exploration. *Acc. Chem. Res.* **2020**, *53*, 2119−2129.
(45) Ma, S.; Shang, C.; Wang, C.-M.; Liu, Z.-P. Thermodynamic Rules for Zeolite Formation from Machine Learning Based Global Optimization. *Chem. Sci.* **2020**, *11*, 10113−10118.
(46) Ma, S.; Liu, Z.-P. Machine Learning for Atomic Simulation and Activity Prediction in Heterogeneous Catalysis: Current Status and Future. *ACS Catal.* **2020**, *10*, 13213−13226.
(47) Kang, P.-L.; Liu, Z.-P. Reaction Prediction via Atomistic Simulation: From Quantum Mechanics to Machine Learning. *iScience* **2021**, *24*, 102013.
(48) Shang, C.; Liu, Z.-P. Stochastic Surface Walking Method for Structure Prediction and Pathway Searching. *J. Chem. Theory Comput.* **2013**, *9*, 1838−1845.
(49) Zhang, X.-J.; Shang, C.; Liu, Z.-P. From Atoms to Fullerene: Stochastic Surface Walking Solution for Automated Structure Prediction of Complex Material. *J. Chem. Theory Comput.* **2013**, *9*, 3252−3260.
(50) Shang, C.; Zhang, X.-J.; Liu, Z.-P. Stochastic Surface Walking Method for Crystal Structure and Phase Transition Pathway Prediction. *Phys. Chem. Chem. Phys.* **2014**, *16*, 17845−17856.
(51) Huang, S.-D.; Shang, C.; Zhang, X.-J.; Liu, Z.-P. Material Discovery by Combining Stochastic Surface Walking Global Optimization with a Neural Network. *Chem. Sci.* **2017**, *8*, 6327−6337.
(52) Huang, S.-D.; Shang, C.; Kang, P.-L.; Liu, Z.-P. Atomic Structure of Boron Resolved Using Machine Learning and Global Sampling. *Chem. Sci.* **2018**, *9*, 8644−8655.
(53) Shang, C.; Huang, S.-D.; Liu, Z.-P. Massively Parallelization Strategy for Material Simulation Using High-Dimensional Neural Network Potential. *J. Comput. Chem.* **2019**, *40*, 1091−1096.
(54) Ma, S.; Shang, C.; Liu, Z.-P. Heterogeneous Catalysis from Structure to Activity via SSW-NN Method. *J. Chem. Phys.* **2019**, *151*, 050901.
(55) Zhang, X.-J.; Shang, C.; Liu, Z.-P. Double-Ended Surface Walking Method for Pathway Building and Transition State Location of Complex Reactions. *J. Chem. Theory Comput.* **2013**, *9*, 5745−5753.
(56) Zhang, X.-J.; Liu, Z.-P. Variable-Cell Double-Ended Surface Walking Method for Fast Transition State Location of Solid Phase Transitions. *J. Chem. Theory Comput.* **2015**, *11*, 4885−4894.
(57) Shang, C.; Liu, Z.-P. Constrained Broyden Minimization Combined with the Dimer Method for Locating Transition State of Complex Reactions. *J. Chem. Theory Comput.* **2010**, *6*, 1136−1144.
(58) Shang, C.; Liu, Z.-P. Constrained Broyden Dimer Method with Bias Potential for Exploring Potential Energy Surface of Multistep Reaction Process. *J. Chem. Theory Comput.* **2012**, *8*, 2215−2222.
(59) Kresse, G.; Joubert, D. From Ultrasoft Pseudopotentials to the Projector Augmented-Wave Method. *Phys. Rev. B: Condens. Matter Mater. Phys.* **1999**, *59*, 1758−1775.
(60) Kresse, G.; Furthmüller, J. Efficient Iterative Schemes for Ab Initio Total-Energy Calculations Using a Plane-Wave Basis Set. *Phys. Rev. B: Condens. Matter Mater. Phys.* **1996**, *54*, 11169−11186.
(61) Perdew, J. P.; Burke, K.; Ernzerhof, M. Generalized Gradient Approximation Made Simple. *Phys. Rev. Lett.* **1996**, *77*, 3865−3868.
(62) Lide, R. D. *CRC Handbook of Chemistry and Physics*, 84th ed.; CRC Press: New York, 2003−2004.

https://doi.org/10.1021/jacs.1c02471
J. Am. Chem. Soc. 2021, 143, 6281−6292

(63) Tang, Q.-L.; Hong, Q.-J.; Liu, Z.-P. CO2 Fixation into Methanol at Cu/ZrO2 Interface from First Principles Kinetic Monte Carlo. *J. Catal.* **2009**, *263*, 114−122.
(64) Xie, W.; Xu, J.; Ding, Y.; Hu, P. Quantitative Studies of the Key Aspects in Selective Acetylene Hydrogenation on Pd(111) by Microkinetic Modeling with Coverage Effects and Molecular Dynamics. *ACS Catal.* **2021**, *11*, 4094−4106.
(65) Yin, Z.; Zhang, Y.; Chen, K.; Li, J.; Li, W.; Tang, P.; Zhao, H.; Zhu, Q.; Bao, X.; Ma, D. Monodispersed Bimetallic PdAg Nanoparticles with Twinned Structures: Formation and Enhancement for the Methanol Oxidation. *Sci. Rep.* **2015**, *4*, 4288.
(66) Kojima, T.; Kameoka, S.; Fujii, S.; Ueda, S.; Tsai, A.-P. Catalysis-Tunable Heusler Alloys in Selective Hydrogenation of Alkynes: A New Potential for Old Materials. *Sci. Adv.* **2018**, *4*, eaat6063.
(67) Cao, Y.; Zhang, H.; Ji, S.; Sui, Z.; Jiang, Z.; Wang, D.; Zaera, F.; Zhou, X.; Duan, X.; Li, Y. Adsorption Site Regulation to Guide Atomic Design of Ni-Ga Catalysts for Acetylene Semi-Hydrogenation. *Angew. Chem., Int. Ed.* **2020**, *59*, 11647.
(68) Niu, Y.; Huang, X.; Wang, Y.; Xu, M.; Chen, J.; Xu, S.; Willinger, M.-G.; Zhang, W.; Wei, M.; Zhang, B. Manipulating Interstitial Carbon Atoms in the Nickel Octahedral Site for Highly Efficient Hydrogenation of Alkyne. *Nat. Commun.* **2020**, *11*, 3324.
(69) Osswald, J.; Giedigkeit, R.; Jentoft, R. E.; Armbrüster, M.; Girgsdies, F.; Kovnir, K.; Ressler, T.; Grin, Y.; Schlögl, R. Palladium−Gallium Intermetallic Compounds for the Selective Hydrogenation of Acetylene: Part I: Preparation and Structural Investigation Under Reaction Conditions. *J. Catal.* **2008**, *258*, 210−218.
(70) Osswald, J.; Kovnir, K.; Armbrüster, M.; Giedigkeit, R.; Jentoft, R. E.; Wild, U.; Grin, Y.; Schlögl, R. Palladium−Gallium Intermetallic Compounds for the Selective Hydrogenation of Acetylene: Part II: Surface Characterization and Catalytic Performance. *J. Catal.* **2008**, *258*, 219−227.

https://doi.org/10.1021/jacs.1c02471
J. Am. Chem. Soc. 2021, 143, 6281−6292